Lab on a Chip

PAPER

View Article Online
View Journal | View Issue

Cite this: *Lab Chip*, 2020, **20**, 4166

Modular microreactor with integrated reflection element for online reaction monitoring using infrared spectroscopy†

Jasper J. A. Lozeman, *[a] Tobias Elsbecker,[a] Sylvie Bohnenn,[a] Hans L. de Boer,[a] Max Krakers,[a] Guido Mul, [b] Albert van den Berg [a] and Mathieu Odijk *[a]

Received 10th July 2020,
Accepted 2nd October 2020

DOI: 10.1039/d0lc00704h

rsc.li/loc

We report on the fabrication of an internal reflection element (IRE) combined with a modular polymer microfluidic chip that can be used for attenuated total reflection (ATR) infrared spectroscopy. The IRE is fabricated from a silicon wafer. Two different polymers are used for the fabrication of the two types of modular microfluidic chips, namely polydimethylsiloxane (PDMS) and cyclic olefin copolymer (COC). The microfluidic chip is modular in the sense that several layers of mixing channels, using the herringbone mixer principle, and reactions chambers, can be stacked to facilitate the study of the desired reaction. A model Paal–Knorr reaction is carried out to prove that the chip works as intended. Furthermore, we highlight the strength of IR spectroscopy as a tool for reaction monitoring by identifying the peaks and showing the different reaction orders at the different steps of the Paal–Knorr reaction. The reduction of the aldehyde groups indicates a (pseudo) first order reaction whereas the vibrational modes associated with the ring formation indicate a zero order reaction. This zero order reaction can be explained with literature, where it is suggested that water acts as a catalyst during the dehydration step, which is the final step in the pyrrole ring formation.

1 Introduction

Online reaction monitoring in microfluidics has the potential to make reaction synthesis cheaper, safer, faster and more environmentally friendly.[1,2] In a review by Jensen *et al.* it is stated that for microreactors to be applicable to more than laboratory applications, sensors must be integrated into the systems. Now, almost 20 years later, only a limited amount of papers have been published regarding online reaction monitoring in microfluidic microreactors, most notably the work by or in association with the groups of H. Gardeniers,[3–7] K. Jensen[2,8] and several others.[9–22] These techniques for direct online measurement operate using different types of sensors, such as mass-spectrometry,[14] fluorescence and UV/vis spectroscopy,[10,15,18,19,21] electrochemistry[4,16,17] and IR/NIR spectroscopy.[3,5,7,9,11–13,20,22] These reported works are often geared towards a specific application and do not expand to broader fields. In our group, we have obtained ample expertise with (modularly designed) microreactor systems.[23–26] Here, we propose a modular microreactor system, making it possible for the microreactor to be adapted to a wide variety of reactions of interest. This is accomplished by changing the number of layers and the polymer material of the reactor chamber. By combining these microreactors with a silicon (Si) internal reflection element (IRE), online attenuated total reflection (ATR) Fourier transform infrared (FTIR) spectroscopy can be performed on-chip. The goal of the authors is to provide a versatile microreactor design enabling online reaction monitoring.

ATR-FTIR is already used in an industrial setting as reaction monitoring technique. Industrial scale reactions can be monitored with ATR fibre optics probes, closely monitoring the progress of the reaction. In a research setting, (ATR)-FTIR, often in combination with MS and NMR, is frequently used to confirm that the expected product is formed by performing measurements *ex situ*.[27] *In situ* reaction monitoring in a research setting is traditionally performed on the macroscale, *e.g.* in large reaction vessels. A major drawback is that mass transport can be slow, for instance between the bulk and the surface of a catalyst. By performing reactions in a microfluidic chip, better control over mass transport, concentrations and temperature can be obtained, and less chemicals can be used.[1] A microfluidic chip can screen reaction conditions, such as ratios of chemicals and concentrations, at higher throughput than classical batch reactions.[1] Additionally, lesser amount of

[a] *BIOS Lab on a Chip Group, MESA+ Institute for Nanotechnology, University of Twente, Drienerlolaan 5, Enschede, The Netherlands.*
E-mail: j.j.a.lozeman@utwente.nl, m.odijk@utwente.nl
[b] *Photocatalytic Synthesis (PCS) Group, Faculty of Science and Technology, University of Twente, Drienerlolaan 5, Enschede, 7522 NB, The Netherlands*

† Electronic supplementary information (ESI) available. See DOI: 10.1039/d0lc00704h

chemicals can be used, which is beneficial for economic, environmental and safety reasons.

In literature, hyphenated ATR-FTIR with microfluidic reaction chambers[3,5,7,12,13] is described. Although these microfluidic devices are well designed, they might be difficult to replicate outside the research group, due to the highly specific and somewhat complex reaction chamber designs. Our simplified fabrication method for this ATR-FTIR chip is easily replicable, compared to the devices mentioned in existing literature. The simplicity and modularity of the chip makes it applicable for a wide variety of reactions. The goal of this work is to show that with limited fabrication techniques, a relatively cheap, modular chip for online reaction monitoring in a microfluidic device equipped with (passive) mixing structures and a reaction chamber can be achieved. To test the functionality of our chip, we performed a Paal–Knorr reaction on-chip. We highlight the strength of IR as a tool for reaction monitoring by identifying the peaks and determining the reaction orders.

2 Materials and methods

Here we describe the fabrication of an internal reflection element (IRE) for ATR-FTIR spectroscopy, combined with a modular microfluidic reaction chamber and mixing channels. The final conceptual design of the modular device can be seen in Fig. 1.

2.1 Fabrication of the silicon IRE

The fabrication of an IRE for ATR-FTIR was achieved by etching facets into a silicon (Si) wafer. The fabrication of the IRE was based on a simplified version of the workflow reported by Herzig-Marx *et al.*,[28] a schematic representation of the fabrication can be seen in the form of a process flow in Fig. 2. In step 1: a 300 nm layer of low-stress silicon rich nitride (SiRN) (Tempress systems, dichlorosilane 77.5 sccm ammonia 20 sccm nitrogen 250 sccm 820–850–870 °C 20 Pa) was deposited by low-pressure chemical vapour deposition on a 525 μm double polished Si wafer. In step 2 photolithography was used to create a layer of Olin Oir 907-17 positive photoresist which acted as a mask for selective SiRN etching. Unlike the previously reported method,[28] where test etching pits were created to align the <100> crystalline plane, our fabrication method aligned the flat of the wafer with the mask using the micro positioning stage of the mask aligner (EVG6200 NT). This way, the same alignment was achieved, while reducing the fabrication steps. After the pattern had been developed, the SiRN was selectively etched as shown in step 3 (PlasmaTherm, 790-series, trifluoromethane 100 sccm oxygen 9 sccm, 5.3 Pa) by use of directional reactive ion etching followed by stripping of the photoresist in step 4. In step 5, the wafer was immersed in a 25 wt% potassium hydroxide (KOH) solution at 70 °C for 7.5 h, which etched the Si wafer until a thin layer of 50 μm Si was left, which created the ATR facets with the dimensions of *l*: 4.15 mm *w*: 10 mm. Finally the remaining SiRN layer was stripped in a 50% hydrofluoric acid solution and the devices were diced (DISCO, DAD3220) from the wafer in step 6, which created the ATR chips with the dimensions *l*: 30 mm *w*: 15 mm *h*: 0.525 mm. Although the devices where made using the MESA$^+$ Nanolab cleanroom facilities, the dimensions of the facets were in the order of several millimetres, therefore the use of a cleanroom is not strictly necessary, enabling the fabrication of cheap Si ATR devices.

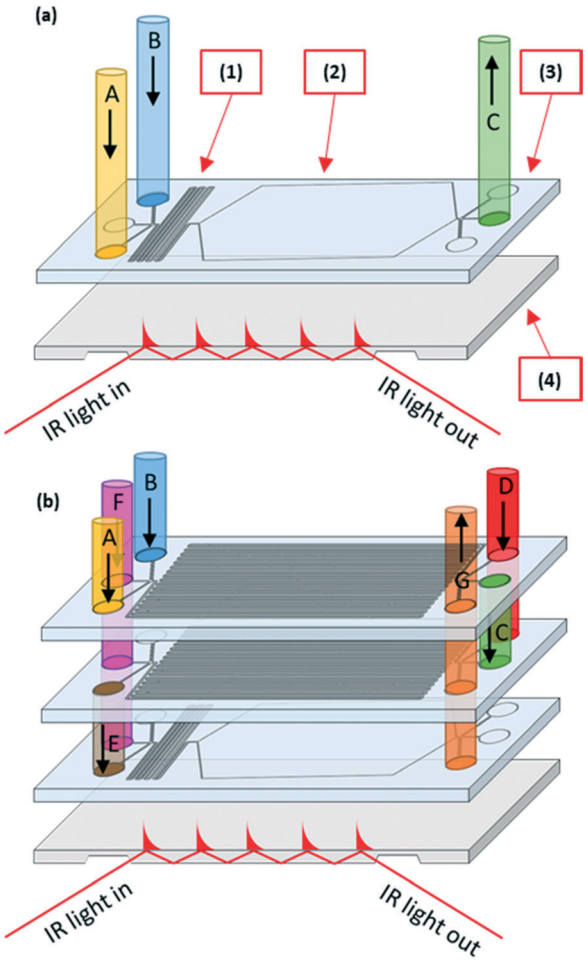

Fig. 1 Two different configurations of the IRE combined with the microfluidic mixer and reaction chamber layers. Several tubings can be connected to the inlets of the microfluidic layer in order to introduce the reactants. a): IRE with a single layer of a combined mixing and reaction chamber. Several tubings, two inlets for introducing the reactants (A and B) and one outlet for the product (C), are connected to the device. Highlighted with numbers are: (1) mixing channels. (2) reaction chamber. (3) polymer microfluidic chip. (4) Si IRE. Chips with the single microfluidic layer which can be used for simple reactions, such as a Paal–Knorr reaction (reaction mechanism shown in Fig. 5) b) Si-ATR device with a three microfluidic layers, which can be used for reactions with more than two reactants. Several tubings are connected to the device, four inlets for introducing the reactants (A, B, D and F) and one outlet for the final product (C). Holes are punched or drilled in two layers allowing the transport of liquid between different layers (C and E).

2.2 Microfluidic chip design

Two polymers have been used to fabricate the modular microfluidic chips. These are: polydimethylsiloxane (PDMS) and

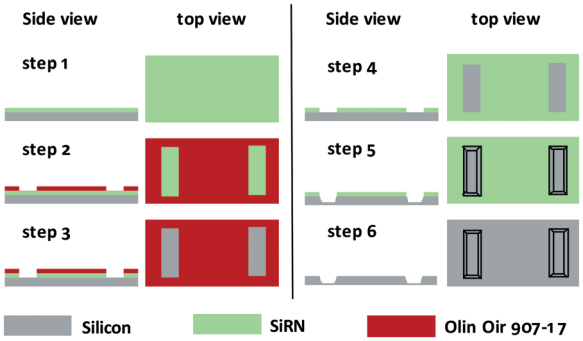

Fig. 2 Process flow for Si-IRE. Step 1–4: Creating SiRN mask for selective KOH etching of Si. Step 5 selective KOH etching of Si to create the facets. Step 6: Dicing of the wafer to obtain the Si-IRE.

cyclic olefin copolymer (COC). These different polymers required different fabrication and bonding techniques, both with their own advantages and disadvantages. An added benefit to using different polymers is their different chemical inertness,[29] allowing the user to change polymers in order to facilitate the requirements of a desired reaction. As show in Fig. 1, the chip consisted of a mixing channel (Fig. 1a, 1) followed by a reaction chamber (Fig. 1a, 2), where the reaction took place. The reaction chamber was shaped as an elongated hexagon, which prevented the formation of air bubbles during filling and prevented the formation of stagnation zones in the corners. The mixing channel was required since the flow was operated in the laminar regime. The mixer ensured that reactants were introduced as a homogenously mixed solution into the reaction chamber. The mixing channels were of the herringbone design, which was first reported by Stroock *et al.*[30] This mixer created a chaotic flow by adding a transverse flow component. In the PDMS design, the herringbone structures were recessed into PDMS. For the COC design the herringbone structures were protruded into the channel.

Several different variations of the mixing and reaction chamber were designed and fabricated (see Fig. S1 and S2†). These variations could be combined by stacking up to three layers on top of each other, accommodating different reaction requirements. The chips had been designed such that the walls cover the sensing area of the ATR device as little as possible, preventing losses due to absorption of the polymer of the microfluidic chip.

2.3 Microfluidic chip fabrication

The PDMS devices were made in a cleanroom facility by use of lithography, containing structures with dimensions in the order of 10 μm. The COC chip was made with a different technique, namely by micromilling, which eliminated the need for a cleanroom facility. This resulted in a lower resolution device, which mostly affected the width of the mixing channels and the size of the herringbone structures. This micromilling technique could also be used for similar polymers such as poly(methyl2-methylpropenoate), poly(oxymethylene), poly(tetrafluoroethylene), polystyrene and polycarbonate. A comparison of the PDMS and COC chip design and material properties is given in Table 1.

2.3.1 PDMS chip. The process flow for the fabrication PDMS chip can be seen in Fig. 3. The PDMS chip was fabricated by soft lithography, starting with a layer of SU-8 (MicroChem NANOTM SU-8100, spin speed: 4000 RPM) followed by a pre-bake (subsequent heating steps: 50 °C 10 min, 65 °C 30 min, 95 °C 35 min) and lithography, producing a mould which defined the negative of the channels/reaction chamber without mixing structures. After exposure, a post exposure bake was performed (subsequent heating steps: 50 °C 10 min, 65 °C 10 min, 75 °C 35 min). Before resist development, a second SU-8 layer was applied on top of the first layer (MicroChem NANOTM SU-8 25, spin speed: 1000 RPM) followed by a pre-bake (subsequent heating steps: 50 °C 10 min, 65 °C 30 min, 95 °C 35 min) which defined the herringbone mixing structures. After exposure, a post exposure bake was performed, (subsequent heating steps: 50 °C 10 min, 65 °C 10 min, 75 °C 35 min) followed by a development step (propylene glycol methyl ether acetate, RER600, ARCH Chemicals) and a hard bake (subsequent heating steps: 50 °C 10 min, 65 °C 10 min, 100 °C 10 min, 120 °C 120 min). The resulting SU-8 mould contained channels and a reaction chamber with a height of 85 μm. The mixing structures on top of the channels added an additional height of 13.6 μm. This fabricated mould could be reused to make a number of PDMS devices. The PDMS was mixed with a cross-linker (Sylgard 184 kit, containing polymer and cross-linker), degassed, (20.000 Pa for 45 min) and casted on the SU-8 structures, followed by curing in an oven at 60 °C for 3 h. Lastly, the PDMS replica was peeled off the structures followed by punching holes in the in- and outlets with a biopsy puncher (ϕ 1 mm). Next, the PDMS was bonded to the Si-IRE or to a second PDMS chip by an activation of the Si or PDMS surface by an oxygen plasma treatment (Cute plasma system, Femto science).

2.3.2 COC chip. In Fig. 4 the process flow of the fabrication for the COC chip is illustrated. The COC chip was fabricated by micromilling (DATRON Neo) a square piece of COC polymer (DENZ Bio-Medical GmbH) with the thickness of 1.0 mm. The designs (Solidworks) for part A and B (see Fig. S2†) were loaded simultaneously in the milling machine after which the program controls the mill (smallest tool used for the most delicate features in this design: ϕ 0.2 mm at 15.000 RPM and a feed rate of 75 mm min^{-1}. Larger tool for

Table 1 Fabrication specifications of the two different polymer chips

Material	Cleanroom	Channel width (μm)	Channel length (mm)	Chemical inertness
PDMS	Yes	200	70	Low
COC	No	600	215	High

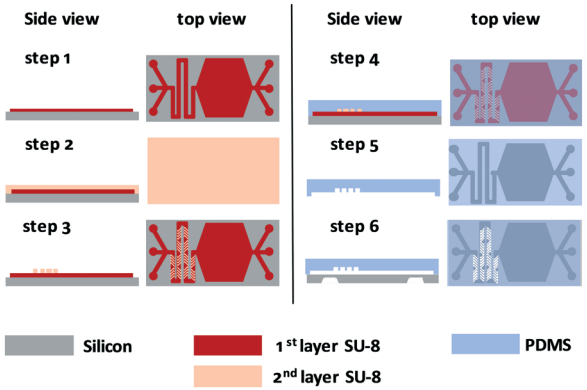

Fig. 3 Process flow fabrication PDMS microfluidic chip. Step 1: SU-8 negative mould for reaction chamber and channels. Step 2 and 3: SU-8 negative mould for mixing channels. Step 4 and 5: Casting the PDMS chip on the SU-8 mould. Step 6: Bonding the PDMS chip on the Si-IRE.

features such as the reaction chamber: a ϕ 1.0 mm at 20.000 RPM and a feed rate of 200 mm min^{-1}). Subsequently the solvent bonding procedure of the COC chip for parts A and B was conducted. The COC chip components are exposed to hexane vapour for 8 minutes in a closed Petri-dish. Next, the parts were pressed together by hand, while being aligned using alignment pins (see Fig. S3†). To complete the bonding, the parts were further pressed together using a hot press (Auto C-PL, Carver, Inc.) operated at 65 °C and a force of 1.1 kN cm^{-2} for 20 min. For bonding COC to the Si IRE unit, NOA-81 (Norland Products Inc.) adhesive was used. A droplet of NOA-81 is deposited on a glass microscopy slide and spin coated at 1500 RPM for 60 s to coat the glass slide with a thin uniform layer of glue. Next, the COC piece was pressed onto the coated glass slide, transferring a thin layer of NOA-81 adhesive. The ATR-device and the COC chip are aligned in the homemade alignment holder, pressure was applied by hand while the device is exposed to UV light (365 nm, 10 s, 400 W cm^{-2}).

2.4 Measurement setup

The chip was mounted in an in-house constructed IR beam aligner. This aligner was used to couple the IR light from the Bruker Vertex 70 into the ATR device and consecutively couple the outgoing beam back into the IR spectrometer. Using a neMESYS syringe pump (CETONI GmbH) fitted with two 5 mL syringes (Hamilton Model 1005-LTN), reagents are introduced into the microfluidic chip. In Fig. S4† images of the setup are shown.

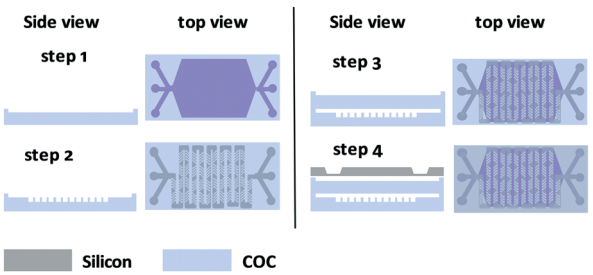

Fig. 4 Process flow fabrication COC microfluidic chip. Step 1 and 2: Micromilling different layers of the COC chip. Step 3: Solvent bonding of two separate COC chips. Step 4: Bonding the COC chip on the Si-IRE by using NOA-81 adhesive.

2.5 Reaction monitoring and data processing

A Paal–Knorr reaction has been performed on-chip, where the reagents hexane-2,5-dione (HD) (Sigma-Aldrich) and butan-1-amine (BA) (Sigma-Aldrich) created the reaction products 1-butyl-2,5-dimethyl-1*H*-pyrrole (BDP) and water. The reaction mechanism as described in literature,[31–34] is shown in Fig. 5. As proof of concept, we use the PDMS chip to perform this reaction. Before the reactants are introduced to the chip, a background scan is made of an empty chip (64 scans, 1 cm^{-1}). Using a syringe pump, the chip was filled with a 1 : 1 mixture of HD (neat) and BA (neat), resulting in a final concentration of 4.3 mol l^{-1} HD and 5.1 mol l^{-1} BA. The time required to fill the chip was 1 min. As soon as the chip is filled, the flow is halted and FTIR spectra are recorded (64 scans, 1 cm^{-1} resolution) every 3.5 minutes for a period of 21 minutes.

Data processing was performed using SpectraGryph. Firstly, the spectra are normalized on the 2930 cm^{-1} CH_2 asymmetric C–H stretch vibration. The spectra where further treated by with a second order derivative filter,[35,36] enhancing the resolution of the spectra and reducing the baseline offset.[35,36] The resulting second order derivative spectra where then integrated and plotted *versus* time. The resulting graph is used to determine the reaction order.

3 Results and discussion

3.1 Fabrication result IRE

In Fig. 6a, a fabricated Si ATR device is shown while in Fig. 6b, a microscope image of one of the facets from the same device is included. As can be seen in this figure, the etched section of the Si surface looks grainy as a result of the KOH treatment. The protected part of the Si device and the facet itself, which are the areas that interact with the light beam, look smooth. From this optical study of the Si surface, we conclude that the deposited SiRN layer is thick and homogenous enough to protect the Si surface from this KOH etching. In the same microscope image, the etching depth can calculated. Based on the preferential etching of the <100> crystalline plane into Si, an etching angle of 54.7° is created resulting in a calculated depth of 0.472 mm. Taking into account the etching rate of KOH of 1 μm min^{-1} and an etching time of 7.5 hours, this closely matches the expected etching depth of 0.475 mm.

3.2 Fabrication result microfluidic chip

In Fig. 7, two images of two different chips are shown. Fig. 7a demonstrates a single PDMS microfluidic chip

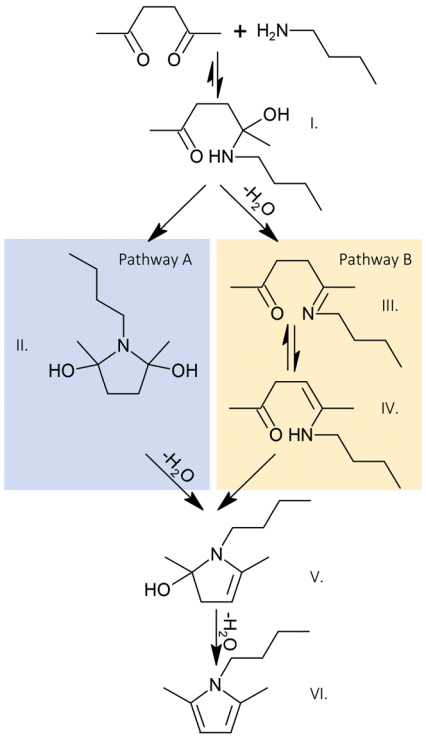

Fig. 5 Reaction mechanism for the Paal–Knorr reaction of hexane-2,5-dione and butan-1-amine to 1-butyl-2,5-dimethyl-1*H*-pyrrole and water side product, as described in the literature.[31–34] Pathway A describes the hemiaminal cyclization step and pathway B describes the enamine cyclization step. The different intermediate products are highlighted with the roman numbers I–V and the final product, BDP, with the roman number VI.

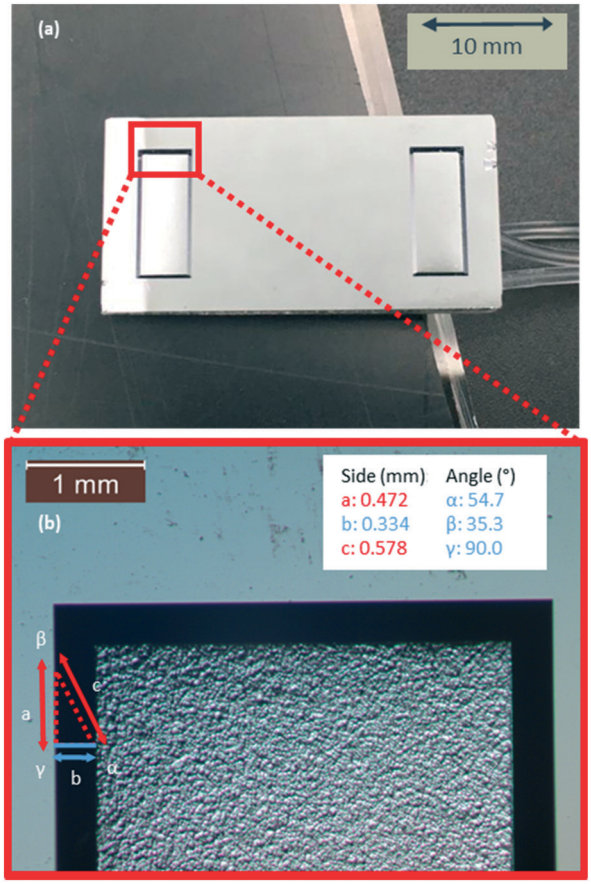

Fig. 6 a) Si ATR-device with the etched facets. b) Microscope image of one of the facets, etching depth confirmed based on the width and angle of the facets.

bonded to a Si-IRE. This chip is a single-layer device, where a mixing channel (length 70 mm) and a reaction chamber are integrated in one PDMS layer. The PDMS bonding procedure has a high success rate. In 6 devices fabricated, none showed any leakage before or after the reaction. Failure is only observed when using too high flow rates (>1 μl s^{-1}), causing the tubing to disconnect from the chip. Fig. 7b shows a double-layered device of COC bonded to a Si-IRE. This device consist of a single COC reaction chamber in the bottom layer and a single mixing channel in the top layer (l: 215 mm). Bonding the several COC layers has a high success rate, rarely showing any leakage or separation. The bonding of the COC to the Si-IRE is more finicky. In most of the cases, the bonding using NOA-81 show some signs of leakage. This is corrected by using a disposable glass pipet to introduce a small amount of NOA-81 to the leakage area. It is then observed that the NOA-81 gets pulled into the opening between the Si-IRE and COC chip, probably by capillary forces. The UV exposure is performed again to cure the NOA-81 and a visual check is performed to determine whether any glue entered the reaction chamber. After this fix, about 75% of the COC-IRE devices show no sign of leakage.

In Fig. 8a and b, microscope images of a PDMS and COC device are shown respectively. As explained in section 2.2, the width of the COC channels is significantly larger than that of the PDMS chip. The herringbone structures are clearly visible and no significant defects can be observed in both the structures and the channels. However, the COC chip clearly has some milling artefacts on the edges of the channels, even after cleaning. In Fig. 8(c and d), a macroscopic image of the PDMS and COC chips is shown respectively. The chips are filled with aqueous solutions containing food dyes in order to determine the mixing performance. Independent of the polymer used and the resulting differences in the width of the channels and grooves of the herringbone, total mixing occurs before the food dyes enter the detection chamber. For the PDMS chips this occurs observed in the second channel, for the COC in the ninth channel (for RGB colour analysis see Fig. S5 and S6†). Therefore it can be concluded that the length of the PDMS channel is, as designed, much longer than the minimum required mixing length. This will guarantee that liquids for the Paal–Knorr reaction, where HD (0.00143 Pa s at 25°) is about 1.5 times more viscous than water (0.00089 Pa s at 25°), will still be properly mixed.

3.3 Measurement results

In Fig. 9a, the spectra of the Paal–Knorr reaction are shown at 3.5 minute interval. In Fig. 9b, the same spectra are shown,

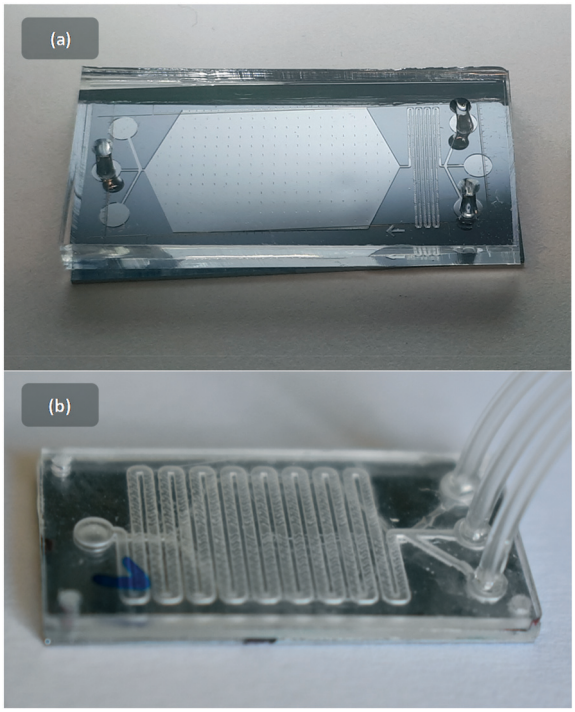

Fig. 7 a) Single layer PDMS chip on Si-IRE. b) double layer COC chip on Si-IRE.

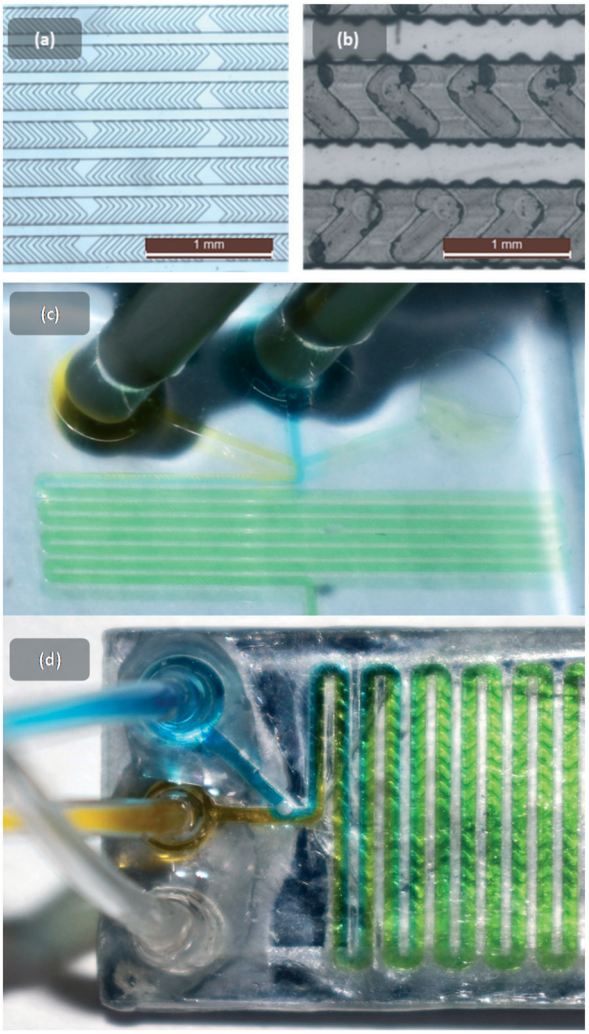

Fig. 8 Mixing channels characterized. a) Mixing channels PDMS chip. Width channel: 200 μm, length channel: 70 mm, depth channel: 85 μm, length herringbone 275 μm, width herringbone 35 μm, depth herringbone 14 μm. b) Mixing channels COC chip. Width channel: 600 μm, length channel: 215 mm, depth channel: 300 μm length herringbone 850 μm, width herringbone 280 μm, depth herringbone 50 μm. c) PDMS chip with food dye. Flow rate of the two different dyes: 0.1 μl s^{-1} for a total flow rate of 0.2 μl s^{-1}. As can be observed, total mixing is achieved in the second mixing channel. d) Figure COC chip with food dye. Flow rate of the two different dyes: 0.1 μl s^{-1} for a total flow rate of 0.2 μl s^{-1}. as can be observed, total mixing is achieved in the ninth mixing channel.

zoomed in on the 1800–900 cm^{-1} region. The most distinct peaks are highlighted with roman numerals. In Fig. 9a, peaks I–IV are highlighted. Table 2 contains the peak assignment. Peak I is a combination of the NH_2 stretch vibration of BA and the OH stretch of H_2O. The NH_2 stretch vibration, with its distinct double peaks (characteristic of a primary amine) is somewhat broadened, possibly due to hydrogen bridging with the ketone groups of HD. Despite the conversion of the primary amine to a tertiary amine, an increase in the peak intensity over time can be observed. This is caused by the formation of H_2O, which has a peak at the same wavelength, and gives two molecules for every single molecule of primary amine being converted. Peak II (CH_2 and CH_3 stretch), peak III (CH_2 stretch) and peak IV (CH_2 stretch of a CH_2–N) show, as expected, little change in peak area. Looking at Fig. 9c, peak V at ~1720 cm^{-1} is highlighted. This peak is the most distinct peak and is largely separated from the other peaks in the spectra. It has a high peak intensity and originates from the C═O stretch vibration of HD. In Fig. 9d, two peaks are highlighted. Peak VI is the total sum of several peaks. Starting from the left, a sharp peak at 1660 cm^{-1} can be observed decreasing over time, possibly NH_2 deformation vibration of BA. Going towards the right, a broad peak increases over time; this can be attributed to the O–H deformation of H_2O. Peak VII, which also increases over time, is the ring skeletal vibration of BDP. In Fig. 9e, the fingerprint region starts and more peak convolution can be observed. Most peaks in this figure are caused by the different C–H_2 and C–H_3 deformation stretch vibrations. Fig. 9f shows the decrease of peak VIII, representing the C–H_2 and C–H_3 deformations adjacent to a C═O stretch vibration. The peak in Fig. 9g, numbered IX, is increasing over time and is probably caused by the C–N deformation of a tertiary amine. Either BDP or the intermediate imine component (Fig. 5 intermediate III) could be responsible for this peak. However, if this peak is caused by the imine intermediate, a shift over time would be expected as the imine is converted to the enamine (Fig. 5 IV) and consequently into the final BDP product. For this reason its highly likely that this peak corresponds to the C–N deformation of BDP. Fig. 9h shows peak X, decreasing over time. This peak is assigned to the skeletal vibration of HD.

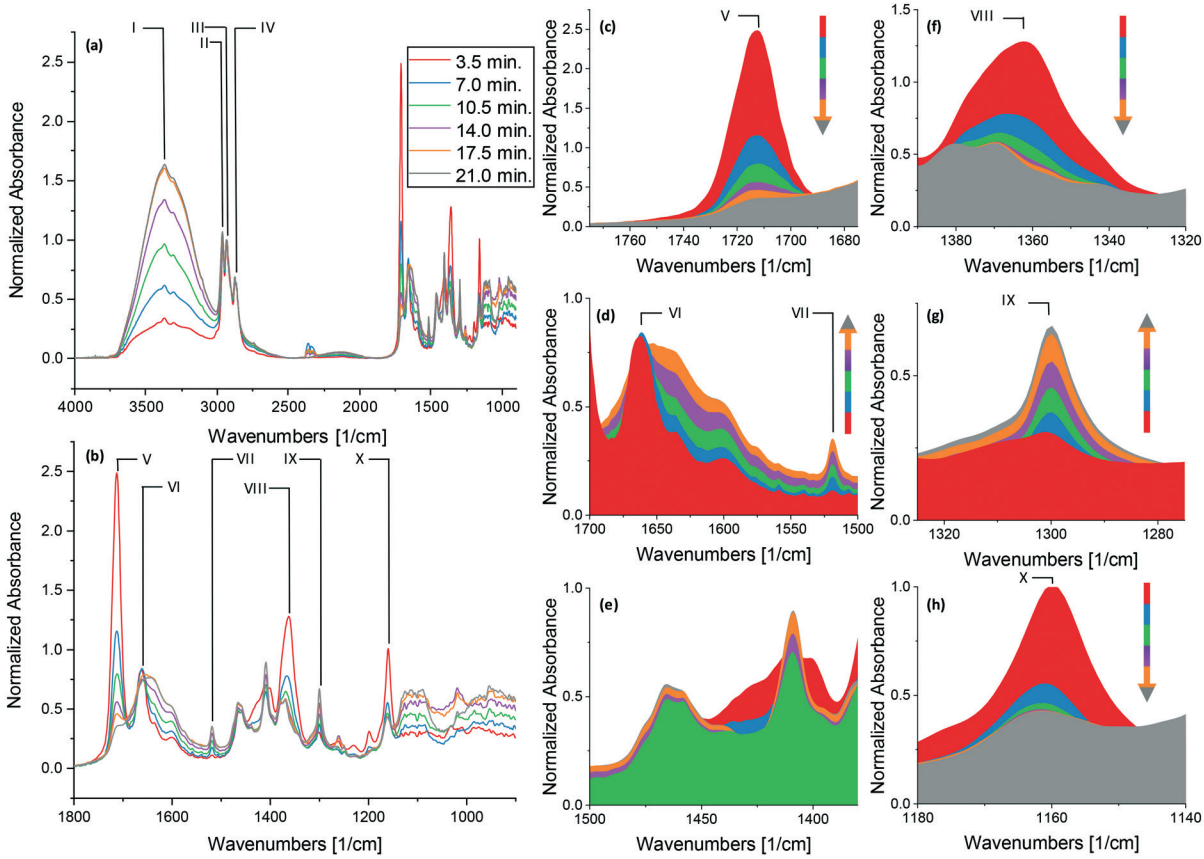

Fig. 9 IR-spectra of the Paal–Knorr reaction. Spectra have been normalized to the CH_3 stretch vibration. a) 6 spectra at 3.5 minute interval. b) Same spectra as in a) extending from 1900 to 900 cm^{-1}. c–h) Enlarged regions of specific peaks of the same spectra. Direction of the arrow indicates if the peaks increase or decrease over time. Line plots of spectra c till h are shown in S7.†

Table 2 Peak assignment

Peak in Fig. 9	Hexane-2,5-dione (cm^{-1})	*n*-Butylamine (cm^{-1})	1-Butyl-2,5-dimethyl-1*H*-pyrrole (cm^{-1})	Water (cm^{-1})	Unknown (cm^{-1})	Peak
I		3370 (ref. 37–39)				NH_2 stretch
I				3350		O–H stretch
I		3300 (ref. 37–39)				NH_2 stretch
	3000 (ref. 39–42)					CH_3 stretch
II	2960 (ref. 39–42)	2960 (ref. 37–39)	2960 (ref. 39 and 43)			CH_3 stretch
III	2930 (ref. 39–42)	2930 (ref. 37–39)	2930 (ref. 39 and 43)			CH_3 stretch
IV		2875 (ref. 37–39)	2875 (ref. 39 and 43)			CH_2–N stretch
V	1715 (ref. 39–42)					C═O stretch
VI					1660	Unknown
				1645		O–H deformation
		1600 (ref. 37–39)				NH_2 deformation
VII			1520 (ref. 39 and 43)			Ring skeletal vibration
		1460 (ref. 37–39)	1460 (ref. 39 and 43)			$C–H_3$/$C–H_2$ deformation
	1410 (ref. 39–42) broad					$C–H_3$/$C–H_2$ deformation
			1410 (ref. 39 and 43) thin			$C–H_3$/$C–H_2$ deformation
		1380 (ref. 37–39)				$C–H_3$ deformation
VIII	1360 (ref. 39–42)					$C–H_3$ deformation
IX			1300 (ref. 39 and 43)			C–N deformation
	1260 (ref. 39–42)					Skeletal vibrations
	1230 (ref. 39–42)					Skeletal vibrations
	1200 (ref. 39–42)					Skeletal vibrations
X	1160 (ref. 39–42)					Skeletal vibrations

In Fig. 10(a–c), the second order derivative of 3 peaks are shown. As one can see in these plots, negligible changes in peak intensity can be observed between the 17.5 min and 21.0 min spectra, suggesting that the reaction has come to completion. In Fig. 10(d–f) plots of the area of this derivative *versus* time have been shown. For these plots, the points at 21.0 min have been left out. The peaks plotted are those most separated in the spectrum and where the vibrational frequency can be assigned to a single molecule. In Fig. 10a, the second order derivative spectra of the C=O stretch vibration peak of HD is shown at different measurement times. The area of these peaks are plotted against time in Fig. 10d, showing an exponential decay of the C=O vibration peak area. This suggest that the intermediate products formed by removal of the C=O bond (Fig. 5. intermediates I and either II or V depending on the pathway) are formed at an exponential rate. This also suggests that this process is a first or pseudo first order reaction. When looking at the ring skeletal vibration of BDP (Fig. 10b) and its increase over time (Fig. 10e), a linear line can be plotted. Looking at Fig. 5, the ring skeletal is formed at the final step to form the end product, suggesting that side intermediate product V is converted into BDP at an linear rate. It also suggest that this process is a zero order reaction. Looking at the C–N deformation peak (Fig. 10c) and the plotted increase over time (Fig. 10f), a linear fit can also be can be made. This suggest that the tertiary amine is formed at an linear rate, indicating that this process is also a zero order reaction. The data in Fig. 10d suggest that the first reaction step in the pyrrole formation by Paal–Knorr is a first order reaction. Since the chemicals used in the current experiment are used in excess, this could also mean that this is pseudo first order reaction. The zero order reaction of the formation of the C–N bond and the BDP ring is more peculiar and suggest that this process is limited by reactant molecules.

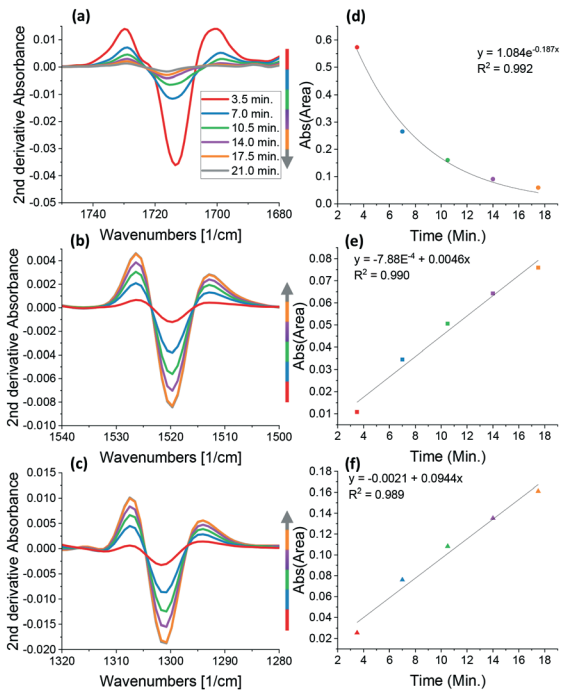

Fig. 10 Second order derivative of 3 peaks. a) C=O stretch vibration. b) Ring skeletal vibration. c) C–N deformation vibration. d) Plotted integrated area of the second order derivative C=O stretch vibration against time. e) Plotted integrated area of the second order derivative ring skeletal vibration against time. f) Plotted integrated area of the second order derivative C–N deformation vibration.

This might be explained by Mothana and Boyd,[33] which states that water is used as a catalyst during the reaction. Catalysis by water takes place primarily during the hydroxyl removal from the diol intermediate and the dehydration step, which occurs for the final two steps in the pyrrole ring formation for pathway A (Fig. 5). Since the reaction is performed with low concentration of water present, zeroth order reaction behaviour is to be expected if pathway A is indeed the pathway of the reaction. The result of these IR measurements seem to be in line with the conclusions made by Mothana and Boyd[33] that water is used as a catalyst, although more research is required to confirm this.

4 Conclusion

We successfully fabricated a modular microfluidic device, which can adapted to the number of steps of the reaction of interest. We show a single layer PDMS chip and a double layer COC chip to highlight the modularity of the device. We prove that the mixer structures function as designed by using a food dye, demonstrating that the mixing channels are overdesigned and therefore suitable for liquids that are more viscous. The microfluidic chip is combined with a Si-IRE that can be used for ATR-FTIR spectroscopy. A model Paal–Knorr reaction has successfully been performed on-chip. We show the strength of IR by highlighting and assigning the most important vibrational frequencies and determining the reaction orders of different steps of the reaction. Finally, the data obtained corresponds to that described in literature,[33] suggesting that water is used as a catalyst during the dehydration step, which is the final step in the pyrrole ring formation.

Author contributions

This section describes the author contributions following the CRediT format. Jasper Lozeman: conceptualization, formal analysis, investigation, methodology, supervision, visualization, writing – original draft. Tobias Elsbecker: conceptualization, investigation, writing – review & editing. Sylvie Bohnenn: conceptualization, investigation, writing – review & editing. Hans de Boer: investigation, writing – review & editing. Max Krakers: investigation, writing – review & editing. Guido Mul writing – review & editing. Albert van den Berg: funding acquisition, supervision, writing – review & editing. Mathieu Odijk: conceptualization, funding acquisition, supervision, writing – review & editing.

Conflicts of interest

There are no conflicts to declare.

Acknowledgements

This work was supported by the Netherlands Center for Multiscale Catalytic Energy Conversion (MCEC), and the Netherlands Organisation for Scientific Research (NWO) Gravitation programme funded by the Ministry of Education, Culture and Science of the government of the Netherlands. The authors would like to thank Klavs Jensen, Baris Unal and Corentin Tregouet for the discussions in the initial phase of the project and Esther Tanumihardja for her input regarding the manuscript preparation.

References

1 K. F. Jensen, *Chem. Eng. Sci.*, 2001, **56**, 293–303.
2 J. S. Moore and K. F. Jensen, *Org. Process Res. Dev.*, 2012, **16**, 1409–1415.
3 A. Susarrey-Arce, R. M. Tiggelaar, R. G. P. Sanders, B. Geerdink, L. Lefferts, J. G. E. Gardeniers and A. van Houselt, *J. Phys. Chem. C*, 2013, **117**, 21936–21942.
4 M. van Leeuwen, E. E. Krommenhoek, J. J. Heijnen, H. Gardeniers, L. A. M. van der Wielen and W. M. van Gulik, *Biotechnol. Prog.*, 2010, **26**, 293–300.
5 E. Karabudak, B. L. Mojet, S. Schlautmann, G. Mul and H. J. G. E. Gardeniers, *Anal. Chem.*, 2012, **84**, 3132–3137.
6 A. Susarrey-Arce, R. M. Tiggelaar, J. G. E. Gardeniers, A. Van Houselt and L. Lefferts, *J. Phys. Chem. C*, 2015, **119**, 24887–24894.
7 A. Susarrey-Arce, R. M. Tiggelaar, M. Morassutto, J. Geerlings, R. G. P. Sanders, B. Geerdink, S. Schlautmann, L. Lefferts, A. van Houselt and J. G. E. Gardeniers, *Sens. Actuators, B*, 2015, **220**, 13–21.
8 J. S. Moore and K. F. Jensen, *Angew. Chem.*, 2014, **126**, 480–483.
9 P. Sagmeister, J. D. Williams, C. A. Hone and C. O. Kappe, *React. Chem. Eng.*, 2019, **4**, 1571–1578.
10 E. A. Abu, S. A. Bryan, C. J. Seliskar and W. R. Heineman, *Electroanalysis*, 2012, **24**, 1517–1523.
11 O. M. Wilkin, P. M. Maitlis, A. Haynes and M. L. Turner, *Catal. Today*, 2003, **81**, 309–317.
12 K. K. Sriram, S. Nayak, S. Pengel, C. F. Chou and A. Erbe, *Analyst*, 2017, **142**, 273–278.
13 A. Aguirre, P. A. Kler, C. L. A. Berli and S. E. Collins, *Chem. Eng. J.*, 2014, **243**, 197–206.
14 X. Hu, Y. Dong, Q. He, H. Chen and Z. Zhu, *J. Chromatogr., B*, 2015, **990**, 96–103.
15 Y. Li, B. Lin, L. Ge, H. Guo, X. Chen and M. Lu, *Nat. Publ. Gr.*, 2016, 1–9.
16 S. Urban, A. Weltin, H. Flamm, J. Kieninger, B. J. Deschner, M. Kraut, R. Dittmeyer and G. A. Urban, *Sens. Actuators, B*, 2018, **273**, 973–982.
17 Y. Lin, Z. Zhang, L. Zhao, X. Wang, P. Yu, L. Su and L. Mao, *Biosens. Bioelectron.*, 2010, **25**, 1350–1355.
18 L. Chen, J. West, P. Auroux, A. Manz, P. J. R. Day, T. Manchester and I. Biocentre, *Anal. Chem.*, 2007, **79**, 9185–9190.
19 M. N. Slyadnev, M. V. Lavrova, M. A. Erkin, V. A. Kazakov and A. A. Ganeev, *J. Anal. Chem.*, 2008, **63**, 192–198.
20 E. L. Martínez Arias, P. Fazzio Martins, A. L. Jardini Munhoz, L. Gutierrez-Rivera and R. MacIel Filho, *Ind. Eng. Chem. Res.*, 2012, **51**, 10755–10767.
21 J. N. Richardson, Z. Aguilar, N. Kaval, S. E. Andria, T. Shtoyko, C. J. Seliskar and W. R. Heineman, *Electrochim. Acta*, 2003, **48**, 4291–4299.
22 R. Richard, B. Dubreuil, S. Thiebaud-Roux and L. Prat, *Fuel*, 2013, **104**, 318–325.
23 M. Odijk, A. Baumann, W. Lohmann, F. T. G. Van Den Brink, W. Olthuis, U. Karst and A. Van Den Berg, *Lab Chip*, 2009, **9**, 1687–1693.
24 F. T. G. G. van den Brink, W. Olthuis, A. van den Berg and M. Odijk, *TrAC, Trends Anal. Chem.*, 2015, **70**, 40–49.
25 R. G. Geitenbeek, J. C. Vollenbroek, H. M. H. Weijgertze, C. B. M. Tregouet, A. E. Nieuwelink, C. L. Kennedy, B. M. Weckhuysen, D. Lohse, A. Van Blaaderen, A. Van Den Berg, M. Odijk and A. Meijerink, *Lab Chip*, 2019, **19**, 1236–1246.
26 F. T. G. van den Brink, T. Wigger, L. Ma, M. Odijk, W. Olthuis, U. Karst and A. van den Berg, *Lab Chip*, 2016, **16**, 3990–4001.
27 P. Y. Bruice, *Organic Chemistry*, Prentice Hall, 2011.
28 R. Herzig-Marx, K. T. Queeney, R. J. Jackman, M. A. Schmidt and K. F. Jensen, *Anal. Chem.*, 2004, **76**, 6476–6483.
29 G. Wypych, *Handbook of Polymers*, Elsevier Science, 2016.
30 A. D. Stroock, S. K. W. Dertinger, A. Ajdari, I. Mezić, H. A. Stone and G. M. Whitesides, *Science*, 2002, **295**, 647–651.
31 V. Amarnath, D. C. Anthony, K. Amarnath, W. M. Valentine, L. A. Wetterau and D. G. Graham, *J. Org. Chem.*, 1991, **56**, 6924–6931.
32 V. Amarnath, K. Amarnath, W. M. Valentine, M. A. Eng and D. G. Graham, *Chem. Res. Toxicol.*, 1995, **8**, 234–238.
33 B. Mothana and R. J. Boyd, *J. Mol. Struct.: THEOCHEM*, 2007, **811**, 97–107.
34 S. Abbat, D. Dhaked, M. Arfeen and P. V. Bharatam, *RSC Adv.*, 2015, **5**, 88353–88366.
35 P. Lasch, *Chemom. Intell. Lab. Syst.*, 2012, **117**, 100–114.
36 B. C. Smith, *Fundamentals of Fourier Transform Infrared Spectroscopy*, CRC Press, Cambridge, 2011.
37 J. J. C. Teixeira-Dias, L. A. E. B. de Carvalho, A. M. A. da Costa, I. M. S. Lampreia and E. F. G. Barbosa, *Spectrochim. Acta, Part A*, 1986, **42**, 589–597.
38 P. K. Kipkemboi, P. C. Kiprono and J. J. Sanga, *Bull. Chem. Soc. Ethiop.*, 2003, **17**, 211–218.
39 E. Pretsch, P. Bühlmann and M. Badertscher, *Structure determination of organic compounds: tables of spectral data*, Springer, 2009.
40 R. L. Hudson, P. A. Gerakines and R. F. Ferrante, *Spectrochim. Acta, Part A*, 2018, **193**, 33–39.
41 L. G. Tensmeyer, R. W. Hoffmann and G. W. Brindley, *J. Phys. Chem.*, 1960, **64**, 1655–1662.
42 G. Dellepiane and J. Overend, *Spectrochim. Acta*, 1966, **22**, 593–614.
43 D. Akbaşlar, O. Demirkol and S. Giray, *Synth. Commun.*, 2014, **44**, 1323–1332.